

# A thermo-metallurgical-mechanical model for selective laser melting of Ti6Al4V

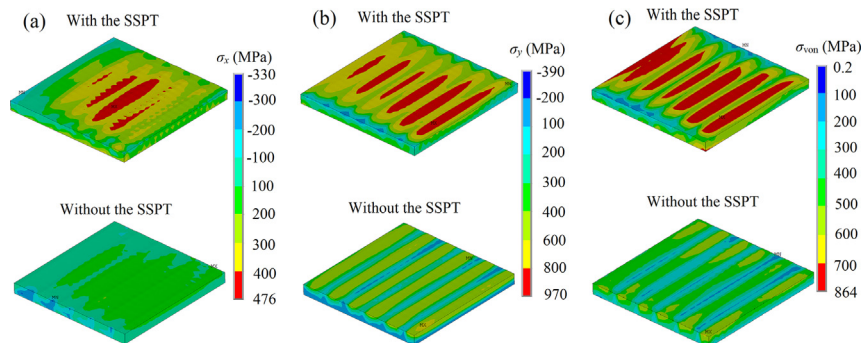
Pengfei Tan, Fei Shen, Biao Li, Kun Zhou \*

Singapore Centre for 3D Printing, School of Mechanical & Aerospace Engineering, Nanyang Technological University, 50 Nanyang Avenue, 639798, Singapore

## HIGHLIGHTS

- A thermo-metallurgical-mechanical coupling model for selective laser melting is developed.
- The model considers powder-liquid-solid transition and solid-state phase transformation.
- The model can predict temperature, solid-state phase and residual stress fields.
- The consideration of solid-state phase transformation reduces tensile stresses and increases compressive stresses.

## GRAPHICAL ABSTRACT



## ARTICLE INFO

### Article history:

Received 26 October 2018  
Received in revised form 21 January 2019  
Accepted 8 February 2019  
Available online 11 February 2019

### Keywords:

3D printing  
Selective laser melting  
Thermo-metallurgical-mechanical model  
Residual stress field  
Solid-state phase transformation

## ABSTRACT

A thermo-metallurgical-mechanical coupling model is developed to predict temperature, solid-state phase and residual stress fields for the multi-track multi-layer selective laser melting process of Ti6Al4V. The model considers the solid-state phase transformation (SSPT) and powder-liquid-solid transition which includes melting, vaporization, solidification, shrinkage and cooling phenomena. The thermal analysis is based on the transient heat conduction problem with a volumetric heat source describing the laser absorption and scattering in the powder bed. The volume fraction evolution of metallurgical phases is determined by temperature history and used to obtain the volumetric change strain due to the SSPT. An elasto-plastic constitutive law considering the strains that are induced by thermal gradients and the SSPT is proposed to evaluate stress fields. Modelling results reveal that the consideration of the SSPT leads to the decrease of tensile residual stresses and increase of compressive residual stresses, and the residual stress component in the scanning direction is larger than the other two stress components.

© 2019 Elsevier Ltd. This is an open access article under the CC BY-NC-ND license (<http://creativecommons.org/licenses/by-nc-nd/4.0/>).

## 1. Introduction

Selective laser melting (SLM), a powder bed fusion technique, uses a high-intensity laser beam to selectively fuse powder particles layer by layer for printing highly-customized and cost-effective products.

However, SLM-printed products suffer from disadvantages such as poor surface finish, thermal distortion and unsatisfactory mechanical strength characteristics [1]. Among these deficiencies, residual stresses, which mainly result from large thermal gradients in the layer-wise additive manufacturing process, may have a detrimental influence on dimensional accuracy and mechanical performance. To reduce such influence, numerical approaches are widely employed to give insight into the evolution of residual stresses as well as transient temperature fields during the manufacturing process.

\* Corresponding author.  
E-mail address: [kzhou@ntu.edu.sg](mailto:kzhou@ntu.edu.sg) (K. Zhou).

Development of a reliable thermo-mechanical coupling model is of prime significance in residual stress analysis since there exists a complex interaction between thermal and mechanical behaviours in the SLM process. The sequentially coupling thermo-mechanical model which consists of a heat transfer analysis and a subsequent stress analysis has been prevalently employed for the SLM process [2–5]. The thermo-mechanical model can provide a guide to study a variety of measures to minimize residual stresses such as process parameters optimization [6], pre-heating and post heat treatment [7–9], and scanning strategy [10–12]. In recent years, researchers have devoted efforts to improving the thermo-mechanical model. Li et al. [13] developed a multi-scale methodology which integrates microscale, mesoscale and macroscale thermo-mechanical models. Also, Mukherjee et al. [14] improved the thermal model for residual stress analysis by considering thermal-fluid effects in the melt pool.

Despite great progress in the current thermo-mechanical model, the metallurgical solid-state phase transformation (SSPT) has not yet been considered for the stress analysis in the SLM process. The SSPT, which is often associated with the change of material properties, volumetric change and transformation-induced plasticity, has been recognized as a crucial factor for the formation of residual stresses for some carbon steels and titanium alloys [15–17]. Pioneering works about the stress analysis with consideration of the SSPT has been conducted in the laser welding process [18–21] and direct laser deposition (DLD) process [17,22]. However, as a powder-bed manufacturing technique, SLM involves more complex physicochemical phenomena such as the laser-powder interaction, powder-liquid-solid transition and volume shrinkage of the powder bed. For a multi-track multi-layer SLM process, the printed product repeatedly undergoes the SSPT due to preheating and reheating from adjacent tracks or layers, which increases the complexity and significance of the phase transformation. Additionally, SLM exhibits a high temperature gradient and rapid solidification and cooling rates, which are of great importance to microstructural phase formation and characteristics [23].

As a two-phase titanium alloy ( $\alpha$  and  $\beta$  phases), Ti6Al4V has attracted extensive attention for SLM owing to its high strength-to-weight ratio, excellent corrosion resistance and good stability in a wide range of working temperature [6,24]. Metallurgical phase compositions of Ti6Al4V in the SSPT are dependent on the temperature history and cooling rate. The phase transformation kinetics are governed by a diffusive transformation of the  $\alpha$  to  $\beta$  phase in the heating process, while the transformation product of the  $\beta$  phase depends on the cooling rate in the cooling process. When the cooling rate is less than around 20 K/s, the  $\beta$  phase decomposes back to the  $\alpha$  phase [25,26]. For a faster cooling rate, the diffusionless transformation process from the  $\beta$  phase to the martensite  $\alpha'$  phase starts to occur. Furthermore, when the cooling rate is larger than 410 K/s, the  $\beta$  phase is fully transformed to the martensite phase  $\alpha'$  [27]. Although the kinetics of the SSPT for Ti6Al4V in the SLM process have been studied [23,28,29], the effects of the SSPT on the thermal stress evolution have not been well understood.

The objective of this work is to investigate the effects of the SSPT on the residual stress evolution during the SLM process of Ti6Al4V. A thermo-metallurgical-mechanical coupling model considering the SSPT is developed to simulate the multi-track multi-layer manufacturing process. The developed model considers the metallurgical SSPT and powder-liquid-solid transition including the melting, vaporization, solidification, shrinkage and cooling processes. The thermophysical and mechanical properties associated with the temperature and metallurgical compositions are taken into account. The temperature field is obtained by solving the heat conduction governing equation with a volumetric heat source describing the laser-powder interaction. An elasto-plastic constitutive relationship considering the thermal strain and volumetric change strain is proposed to evaluate stress fields.

## 2. Thermo-metallurgical-mechanical coupling model development

This section introduces how to develop the thermo-metallurgical-mechanical coupling model for the SLM process. In the coupling procedure, the temperature field is first obtained by solving transient heat conduction and then used to evaluate the metallurgical solid-phase field. Subsequently, the temperature and solid-state phase fields are imported into the mechanical analysis model to obtain thermal strain and volumetric change strain, respectively. A detailed coupling procedure is illustrated by the flowchart in Fig. A1 of Appendix A. The coupling model is developed by finite element method (FEM) in the ANSYS parametric design language.

### 2.1. Thermo-metallurgical model

#### 2.1.1. Heat conduction governing equation

A three-dimensional transient heat conduction governing equation with temperature-dependent material properties and the volumetric heat source is expressed as [30]

$$\begin{cases} \rho \frac{\partial H}{\partial t} = \nabla \cdot [k \nabla(T)] + Q_V, & t > 0, \\ T = T_0, & t = 0 \end{cases}, \quad (1)$$

where  $T$  is the temperature at point  $(x, y, z)$  at time  $t$ ;  $\rho$ ,  $H$  and  $k$  are the temperature-dependent density, enthalpy and thermal conductivity, respectively;  $Q_V$  is the volumetric heat source. The air natural convection and radiation to the ambient environment on the top surface of the powder bed can be expressed by [18].

$$-k \frac{\partial T}{\partial z} = \delta \omega (T^4 - T_\infty^4) + h_{\text{con}}(T - T_\infty), \quad (2)$$

where  $\delta$  is the Stefan-Boltzmann constant taken as  $5.67 \times 10^8$ ,  $\omega$  is the emissivity,  $T_\infty$  is the ambient temperature taken as 298 K, and  $h_{\text{con}}$  is the heat convection coefficient ( $\text{W}/(\text{m}^2 \cdot \text{K})$ ). Other surfaces are assumed to be under thermal insulating boundary conditions.

Due to the porosity in the powder bed, the laser radiation can be absorbed or scattered by powder particles and the substrate. Based on the interaction model of the laser beam and powder particles, the volumetric heat source is expressed as [31].

$$Q_V(x, y, z) = -\gamma S_0(x, y) \frac{dq(\xi)}{d\xi}, \quad S_0(x, y) = \frac{2P}{\pi r_0^2} e^{-\frac{2(x^2+y^2)}{r_0^2}}, \quad (3)$$

where  $\gamma$  is the extinction coefficient, the dimensionless coordinate  $\xi = \gamma z$  denotes the extinction thickness along the  $z$  direction,  $S_0(x, y)$  is the Gauss surface distribution of the laser energy,  $P$  is the laser power,  $r_0$  is the laser beam radius and the normalized laser irradiance  $q$  is given by Eqs. (B1) and (B2) in Appendix B.

#### 2.1.2. Modelling solid-state phase transformation

Ti6Al4V with both  $\alpha$  and  $\beta$  phases may undergo the SSPT during the heating and cooling processes. A schematic of the volumetric change due to the SSPT during the heating and cooling processes is given in Fig. 1. When the temperature reaches the transformation temperature  $B_s$  during the heating process, the  $\alpha$  phase starts to be transformed to the  $\beta$  phase. Since the unit cell volume of the  $\beta$  phase is larger than that of the  $\alpha$  phase, the material volume decreases with the increasing temperature. During the cooling process, when the temperature is lower than the transformation temperature  $M_s$ , the material volume increases in the phase transformation of the  $\beta$  to  $\alpha$  (or  $\alpha'$ ).

During the heating process, the volume fraction of the  $\beta$  phase is given by the Castro model [32]:

$$f_\beta(T) = \begin{cases} 0.075 + 0.92 \exp(-0.0085(B_f - T)), & 298 \text{ K} < T < B_f \\ 1, & T > B_f \end{cases}, \quad (4)$$

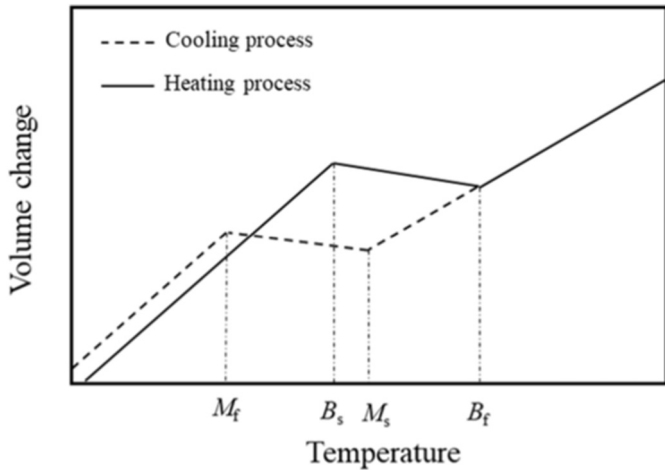


Fig. 1. Schematic of the volumetric change due to the SSPT.

where the finish temperature  $B_f$  of the  $\alpha$  to  $\beta$  phase transformation is 1253 K. Due to the high cooling rate in the SLM process, the diffusive transformation from the  $\beta$  phase to the  $\alpha$  phase is suppressed and the

$\beta$  phase is completely converted to the martensite  $\alpha'$  phase [25,33]. The volume fraction of the martensite  $\alpha'$  phase is obtained by the Koistinen-Marburger equation [34]:

$$f_{\alpha'}(T) = \begin{cases} f_{\beta}'(1 - \exp(-0.015(M_s - T))), & T < M_s \\ 0, & T > M_s \end{cases} \quad (5)$$

where  $f_{\beta}'$  is the initial volume fraction of the  $\beta$  phase in the martensite transformation and the transformation temperature  $M_s$  is taken to be 923 K in this model. The phase volume fractions during heating and cooling processes are plotted in Fig. 2).

A schematic of the SSPT in the multi-track multi-layer SLM process is shown in Fig. 3. A layer of powder particles is initially spread on the substrate (see Fig. 3(a)). The main phase composition of the powder and substrate is the  $\alpha$  phase. In (b), when the first track is scanned by the laser beam, the heat affected zone of the powder layer and substrate with a temperature of over 1253 K is transformed to the  $\beta$  phase. Due to the reheating from the first track, some powder particles in the second track are also transformed to the  $\beta$  phase. When the second track is scanned, the two-track powder layer and one part of the substrate becomes the  $\beta$  phase as given in (c). After a short cooling time at the end of the first layer, the martensite phase transformation occurs in the zone with a temperature lower than 923 K as given in (d). A repeated process of (a)–(d) on the second layer is given in (e)–(h). It is

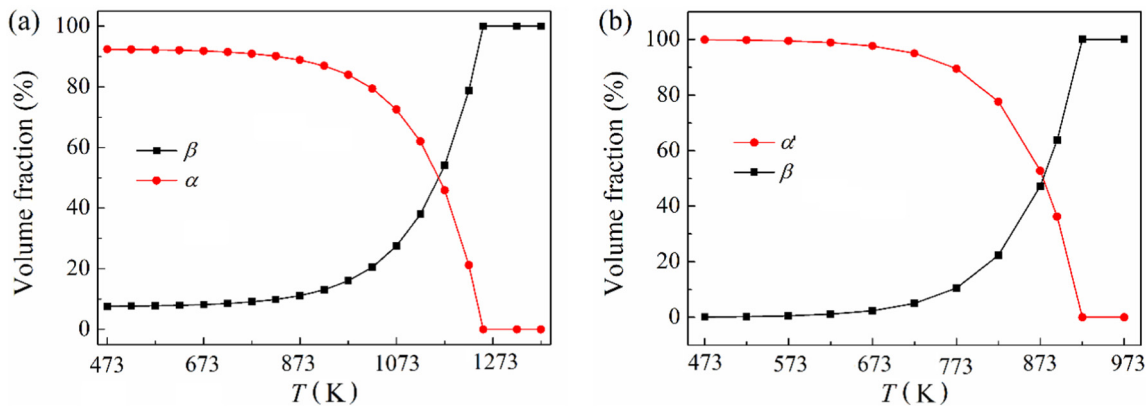


Fig. 2. Phase volume fractions during (a) heating and (b) cooling processes.

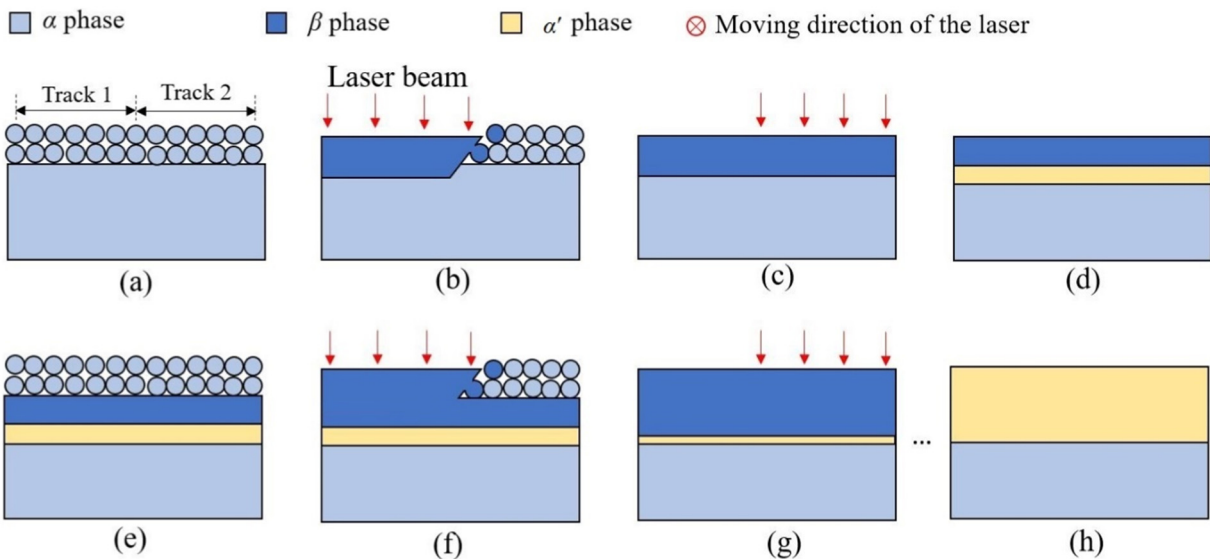


Fig. 3. Schematic of the SSPT in the multi-track multi-layer SLM process: (a) a layer of powder particles is spread; (b) the first track is scanned; (c) the second track is scanned; (d) after cooling down at the end of first layer; (e)–(h): a repeated process of (a)–(d) on the second layer.

observed from (f) and (g) that a portion of the zone with the martensite  $\alpha'$  phase is transformed to the  $\beta$  phase due to reheating from the second layer. After cooling down to the ambient temperature, the printed part becomes martensite  $\alpha'$  phase, as illustrated in (h).

## 2.2. Mechanical model

In the mechanical model, temperature and solid-state phase fields obtained from the previous thermo-metallurgical model are used as input parameters to evaluate the thermal strain and volumetric change strain, respectively. The total strain increment  $d\epsilon^{\text{Total}}$  is expressed by

$$d\epsilon^{\text{Total}} = d\epsilon^e + d\epsilon^p + d\epsilon^{\text{th}} + d\epsilon^{\text{tr}}, \quad (6)$$

where  $d\epsilon^e$  is the elastic strain increment,  $d\epsilon^p$  is the plastic strain increment,  $d\epsilon^{\text{th}}$  is the thermal strain increment and  $d\epsilon^{\text{tr}}$  is the volumetric change strain increment due to the SSPT.

The plastic strain increment is given by considering the flow plasticity:

$$d\epsilon^p = d\lambda \left\{ \frac{\partial f}{\partial \sigma} \right\}, \quad (7)$$

where  $\lambda$  is the hardening parameter,  $\sigma$  is the stress tensor and the yield function  $f$  is obtained by the von Mises yield criterion:

$$f = \sigma_{\text{von}} - \sigma_{\text{yield}}, \quad (8)$$

where  $\sigma_{\text{yield}}$  and  $\sigma_{\text{von}}$  are the yield stress and von Mises stress, respectively. The thermal strain increment is expressed as

$$d\epsilon^{\text{th}} = \alpha_T \Delta T, \quad (9)$$

where  $\alpha_T$  is the coefficient of thermal expansion.

The volumetric change strain increment is given by [26].

$$d\epsilon^{\text{tr}} = \epsilon^{\Delta V}(T) \Delta f_i(T), \quad (10)$$

where  $\epsilon^{\Delta V}$  is the volumetric change strain with a full SSPT and  $f_i(T)$  is the phase volume fraction. The volumetric change strain  $\epsilon^{\Delta V}$  can be determined by the lattice parameter of crystal structures for  $\alpha$  and  $\beta$  phases [26,35,36]:

$$\epsilon^{\Delta V} = \frac{\sqrt[3]{V_\beta} - \sqrt[3]{V_\alpha}}{\sqrt[3]{V_\alpha}}, \quad (11)$$

where  $V_\alpha$  and  $V_\beta$  are unit cell volumes of  $\alpha$  and  $\beta$  phases, respectively. The unit cell volumes of  $\alpha$  and  $\beta$  phases and the volume change strain  $\epsilon^{\Delta V}$  are plotted in Fig. 4.

The volumetric change strain is obtained for the heating and cooling processes by substituting the volume fractions given in Eqs. (4) and (5) to Eq. (10):

$$d\epsilon^{\text{tr}} = \begin{cases} \alpha_h \Delta T, & \text{Heating} \\ \alpha_c \Delta T, & \text{Cooling} \end{cases}, \quad (12)$$

where

$$\begin{cases} \alpha_h = -0.00782 \exp[-0.0085(1253-T)] \epsilon_h^{\Delta V}(T), & 473 \rightarrow 1253 \text{ K} \\ \alpha_c = -0.015 \exp[-0.015(923-T)] \epsilon_c^{\Delta V}(T), & 473 \leftarrow 923 \text{ K} \end{cases} \quad (13)$$

Since both the thermal strain and volumetric change strain are a function of the temperature gradient  $\Delta T$ , they can be combined:

$$d\epsilon^{\text{th}} + d\epsilon^{\text{tr}} = \begin{cases} (\alpha_h + \alpha_T) \Delta T, & \text{Heating} \\ (\alpha_c + \alpha_T) \Delta T, & \text{Cooling} \end{cases} \quad (14)$$

Hence, the SSPT is considered in the mechanical analysis by incorporating the volumetric change strain into the thermal strain in the FEM model.

## 2.3. Volume shrinkage of the powder bed

The volume of the powder bed is decreased after the powder particles are melted by the laser beam. The volume decrease results from the volume shrinkage of the porous powder layer and vaporization. The vaporized metal can be neglected compared with the volume shrinkage. Hence, the volume shrinkage is 40% of the powder bed volume because the porosity of the powder bed is assumed to be 0.4 [37]. A detailed multi-step algorithm for the multi-track multi-layer SLM process considering the volume shrinkage is discussed in our previous work [5]. The volume decrease is simulated by activating and deactivating elements by the element birth and death technique in ANSYS software. After the volume of the powder bed is reduced, the top surface of the printed part is assumed to be flat. The thermophysical properties of the materials including the density, heat conductivity and enthalpy are associated with the volume shrinkage. The material properties are changed from powder particles to the bulk material as the temperature is over the melting point. Since the powder particles have no mechanical effect on the

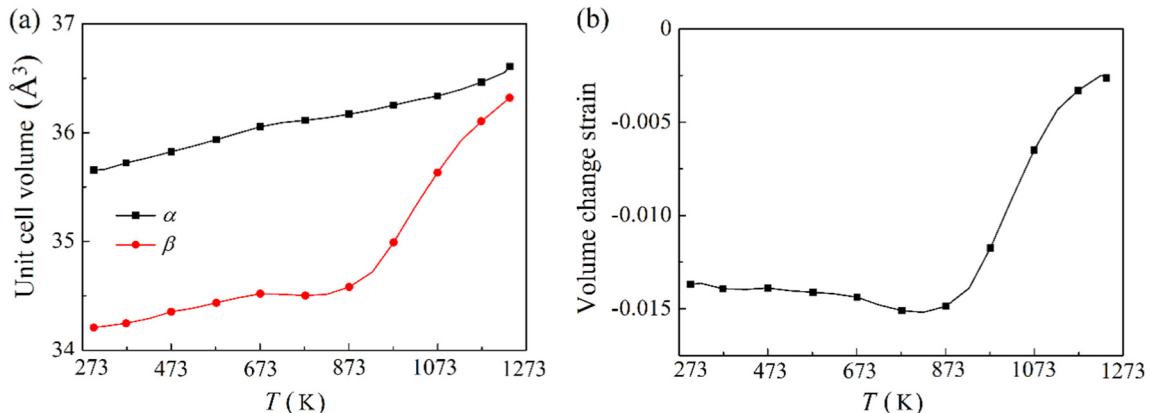


Fig. 4. (a) Unit cell volumes for  $\alpha$  and  $\beta$  phases and (b) volumetric change strain with a full SSPT [26].

printed part, the elements of fresh powder particles are deactivated in the mechanical analysis.

2.4. Material properties

The thermophysical properties used in the coupling model include thermal conductivity, density and enthalpy for powder particles and bulk material. The density  $\rho_p$  is a function of the powder porosity:

$$\rho_p = \begin{cases} (1-\varphi)\rho_b, & T < T_m \\ \rho_b, & T > T_m \end{cases}, \tag{15}$$

where the porosity  $\varphi$  is 0.4 [37], the melting point  $T_m$  is 1923 K and  $\rho_b$  is the density of the bulk material. The effective thermal conductivity  $k_p$  of the powder bed is estimated as [38].

$$\frac{k_p}{k_a} = (1-\sqrt{1-\varphi}) \left(1 + \frac{\varphi k_r}{k_a}\right) + \sqrt{1-\varphi} \left[ \frac{2}{1-k_a/k_b} \left(\frac{k_b}{k_a} \ln(k_b/k_a) - 1\right) + \frac{k_r}{k_a} \right], \tag{16}$$

where  $k_a$  is the thermal conductivity of air,  $k_b$  is the thermal conductivity of the bulk material and  $k_r$  is the thermal conductivity portion due to radiation among powder particles:

$$k_r = 4F\delta T^3 d_r, \tag{17}$$

where  $\delta$  is the Stefan-Boltzmann constant,  $d_r$  is the average diameter of powder particles and  $F$  is the view factor which is taken as 1/3. To consider melting and vaporization processes, the latent heat is directly added to the enthalpy. The latent heat is taken as 286 kJ/kg for melting and 9830 kJ/kg for vaporization [16,26,39]. The temperature-dependent

thermophysical properties of the Ti6Al4V powder particles and bulk material are depicted in Fig. 5.

The temperature-dependent mechanical properties of Ti6Al4V, including the Young's modulus  $E$ , Poisson ratio  $\nu$ , the coefficient of thermal expansion (CTE)  $\alpha_T$ , yield stress  $\sigma_{yield}$  and tangent modulus  $E_T$ , are plotted in Fig. 6. The tangent modulus is assumed to be about 1/20 of the Young's modulus [38]. A bilinear stress-strain constitutive relation is used for the plastic deformation as shown in Fig. 7, which requires the initial yield stress  $\sigma_{yield}$  and tangent modulus  $E_T$  as input parameters.

3. Results and discussion

In this section, the temperature, solid-state phase and residual stress fields are analyzed and the effects of the SSPT on residual stresses are investigated based on the thermo-metallurgical-mechanical coupling model.

3.1. Temperature field

The thermal model is validated by comparing the width and depth of the simulated melt pool with experimental results. The liquid-solid phase distributions in the  $x$ - $z$  cross section of the powder layer and substrate with various powers from 20 to 80 W are shown in Fig. 8. The solid and liquid phases are represented by blue and red colors, respectively. By considering the volume shrinkage of the powder bed, the width and depth of the melt pool is calculated by

$$\begin{cases} \text{Width} = w \\ \text{Depth} = \begin{cases} d-d \times \varphi, & d \leq h \\ d-h \times \varphi, & d > h \end{cases} \end{cases}, \tag{18}$$

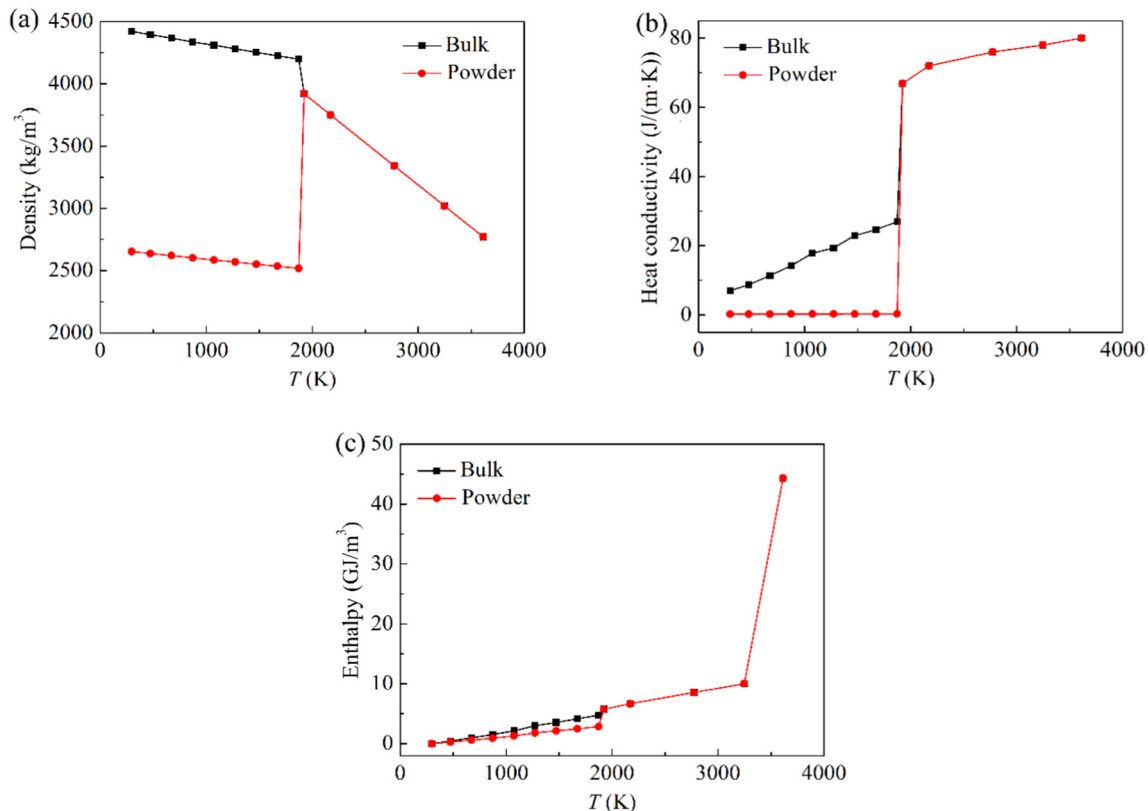


Fig. 5. Thermophysical properties of the Ti6Al4V bulk and powder particles: (a) density, (b) heat conductivity and (c) enthalpy [40,41].

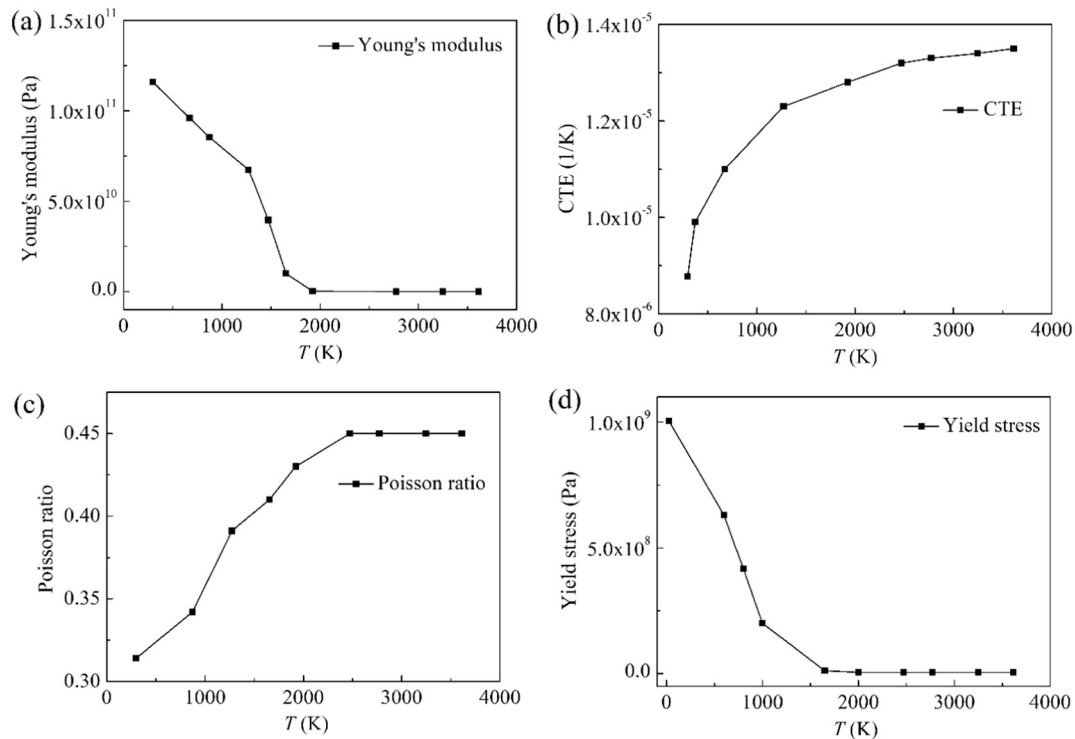


Fig. 6. Mechanical properties for Ti6Al4V: (a) Young's modulus, (b) coefficient of thermal expansion, (c) Poisson ratio and (d) yield stress [3,4].

where  $w$  is the width of the melt pool,  $d$  is the depth of the molten powder bed and substrate,  $h$  is the depth of the molten powder bed and  $\varphi$  is the powder porosity. The simulation has been carried out with a scanning velocity of 200 mm/s and a laser beam radius of 26  $\mu\text{m}$ . The comparison between modelled melt pool sizes and experimental results [42] is illustrated in Fig. 9. From the comparison, the depth and width of the melt pool predicted by the model shows good agreement with the experimental results.

The mesh of the FEM model and scanning pattern for a multi-layer SLM process are shown in Fig. 10. A fine mesh is used for the four-layer printed part and the heat affected zone of the substrate. A unidirectional scanning pattern is adopted within one layer and the scanning directions between two layers are orthogonal. The material of both the

substrate and powder layer is Ti6Al4V. A modelling scheme for the multi-layer SLM process considering the volumetric decrease due to volume shrinkage of the powder bed is reported in our previous paper [5]. The modelling process parameters are listed in Table 1. The temperature evolution for a four-layer printing process is given in Fig. 11. After each layer is finished, the cooling time is 0.1 s. The scanned region by the laser beam becomes thinner due to the consideration of volume shrinkage. Heat diffusion from the heated region to the surrounding fresh powder particles is slow because heat conductivity is low in the powder bed.

### 3.2. Solid-state phase field

The temperature and  $\beta$  phase fields in the  $x$ - $z$  and  $y$ - $z$  cross sections for a one-track printing process are demonstrated in Fig. 12. The powder bed consists of 92.5%  $\alpha$  phase and 7.5%  $\beta$  phase at initial condition according to the Castro model in Eq. (4). The  $\alpha$  phase starts to become the  $\beta$  phase with increasing temperature. As the temperature is higher than  $B_f = 1253$  K, the  $\alpha$  phase is fully transformed to the  $\beta$  phase. The material above around  $-40$   $\mu\text{m}$  in the  $z$  direction is completely transformed to the  $\beta$  phase around the scanned region by the laser beam. The volume fraction of the  $\beta$  phase gradually decreases in the region further away from the heat affected zone.

The evolution of the solid-state phase fields for a three-track printing process is shown in Fig. 13. In the first track as shown in (a), the material with the temperature of over 1253 K is fully transformed to the  $\beta$  phase and the region with lower temperature is a combination of  $\alpha$  and  $\beta$  phases. The martensite  $\alpha'$  phase does not occur at this moment. When the second track is being scanned, the first-track region mainly contains the  $\beta$  phase because the temperature in this region is still higher than the martensitic transformation temperature (923 K). Only a small region around the edge of the heat affected zone in the substrate undergoes the martensitic transformation. When the third track is being scanned, the region with the  $\beta$  phase increases and more  $\alpha'$  phase occurs at the bottom of the first-track heated region. After cooling down,

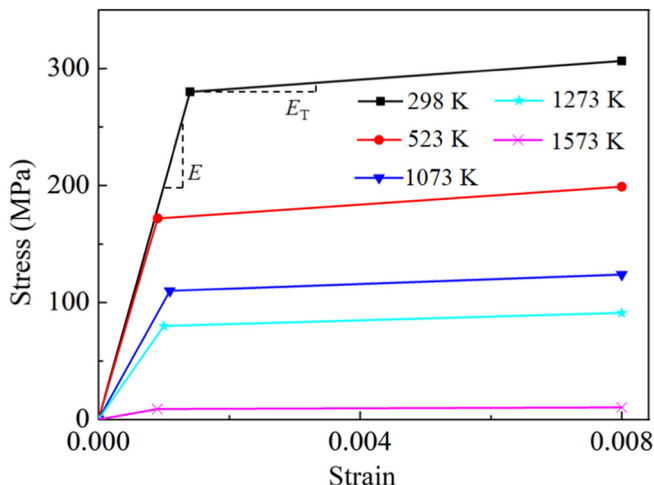


Fig. 7. A bilinear temperature-dependent constitutive relationship for Ti6Al4V [3,4].

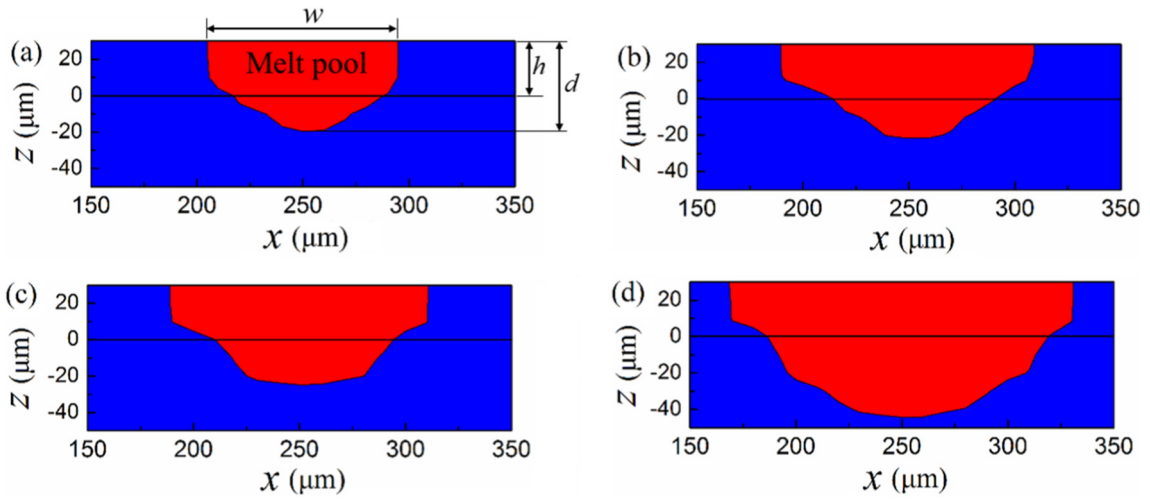


Fig. 8. Liquid-solid phase field in the  $x$ - $z$  cross section of the powder bed and substrate with various powers: (a) 20 W, (b) 40 W, (c) 60 W and (d) 80 W.

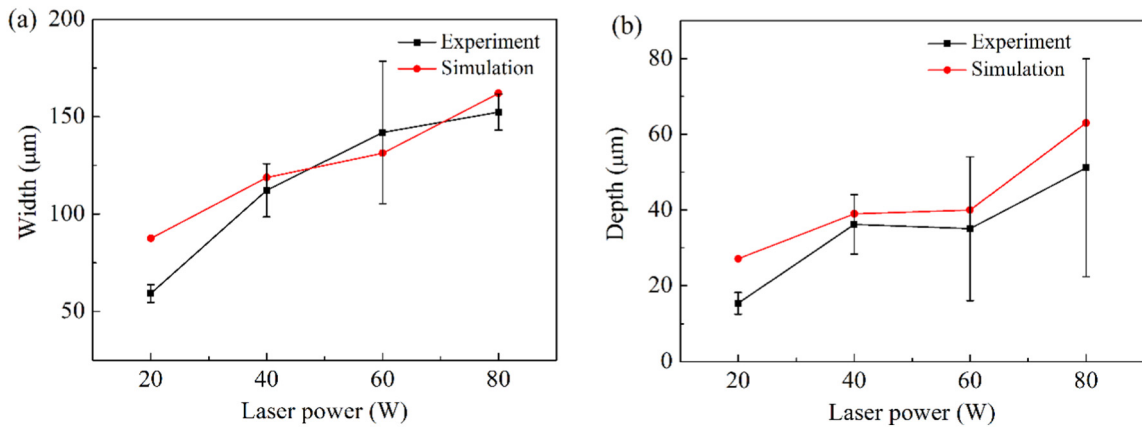


Fig. 9. Comparison of the (a) width and (b) depth of the simulated melt pool with experimental results via the laser power.

most of the  $\beta$  phase in the heated zone is fully transformed to the  $\alpha'$  phase and the region around the edge of the heat affected zone is composed of  $\alpha$  and  $\alpha'$  phases.

The evolution of the temperature and phase volume fraction  $f_\beta$  at the central point of the first track on the top surface of the substrate for the three-track printing process is given in Fig. 14. Three peak points occur

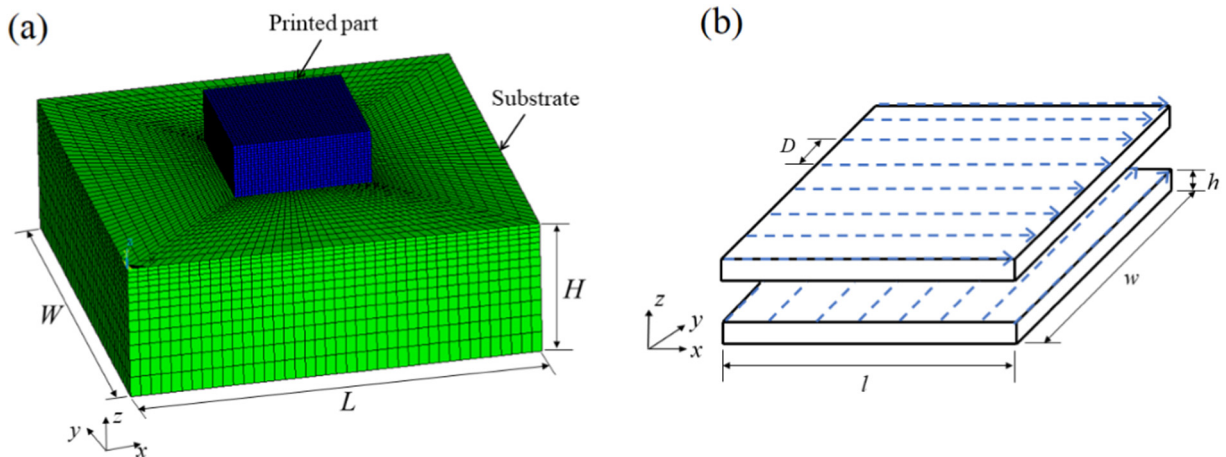


Fig. 10. (a) Mesh of the FEM model and (b) scanning pattern for a multi-layer SLM process.

**Table 1**  
Modelling process parameters for a multi-layer SLM process.

Parameters	Value
Layer thickness $h$ ( $\mu\text{m}$ )	50
Laser beam radius $r_0$ ( $\mu\text{m}$ )	60
Laser power $P$ (W)	100
Laser scan speed $v$ (mm/s)	600
Ambient temperature $T_\infty$ (K)	298
Hatch distance $D$ ( $\mu\text{m}$ )	72
Substrate $L \times W \times H$ ( $\text{mm}^3$ )	$1.5 \times 1.5 \times 0.5$
Powder layer $l \times w \times h$ ( $\text{mm}^3$ )	$0.5 \times 0.5 \times 0.05$

in the temperature history because the point is heated three times while three tracks are scanned by the laser beam sequentially. The peak temperature decreases because the laser beam is gradually moving away from the point. When the laser beam reaches the point, the temperature dramatically increases to 2480 K and the  $\alpha$  phase completely becomes

the  $\beta$  phase at the same time. Then, the point remains in the  $\beta$  phase until the three tracks are scanned. After the scanning is finished, the temperature at the point gradually decreases to the martensitic transformation temperature  $M_s$ . The  $\beta$  phase can be fully transformed to the martensite  $\alpha'$  phase due to the fast cooling rate.

3.3. Residual stress field

In this case, the stress fields for a one-layer printing process are first investigated. The unidirectional scanning strategy with a hatch distance  $D = 1.2r_0$  is used. The printing process parameters including laser parameters and the powder layer thickness are the same as those listed in Table 1 for the multi-layer printing process. In addition, the substrate plate is fixed for the mechanical analysis:

$$\begin{cases} w = 0, & \text{at } z = -H \\ u = 0, & \text{at } x = 0 \text{ and } W, \\ v = 0, & \text{at } y = 0 \text{ and } L \end{cases} \quad (19)$$

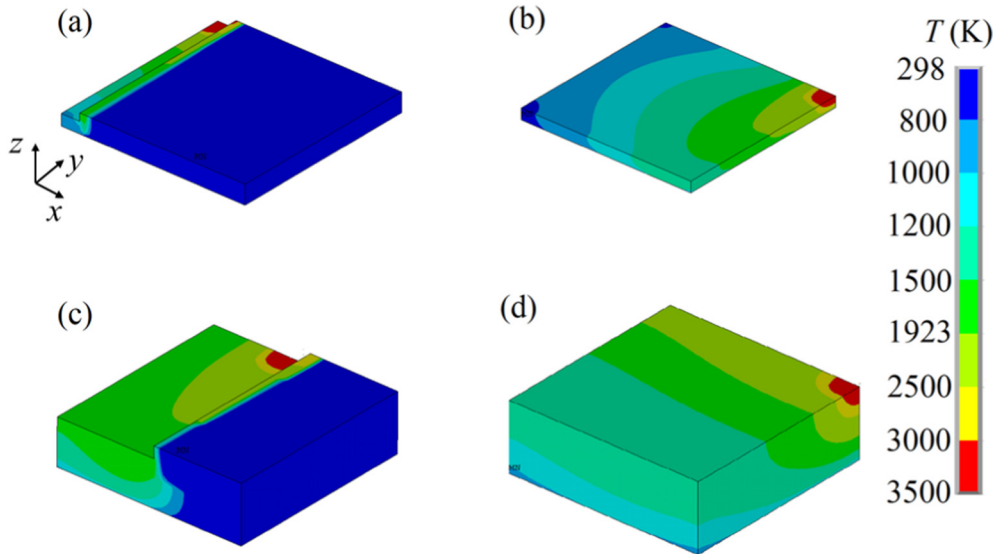


**Fig. 11.** Evolution of the temperature fields for a four-layer SLM process: (a) at the end of the first track, (b) at the end of the first layer, (c) at the middle time of the third layer and at the end of the fourth layer.

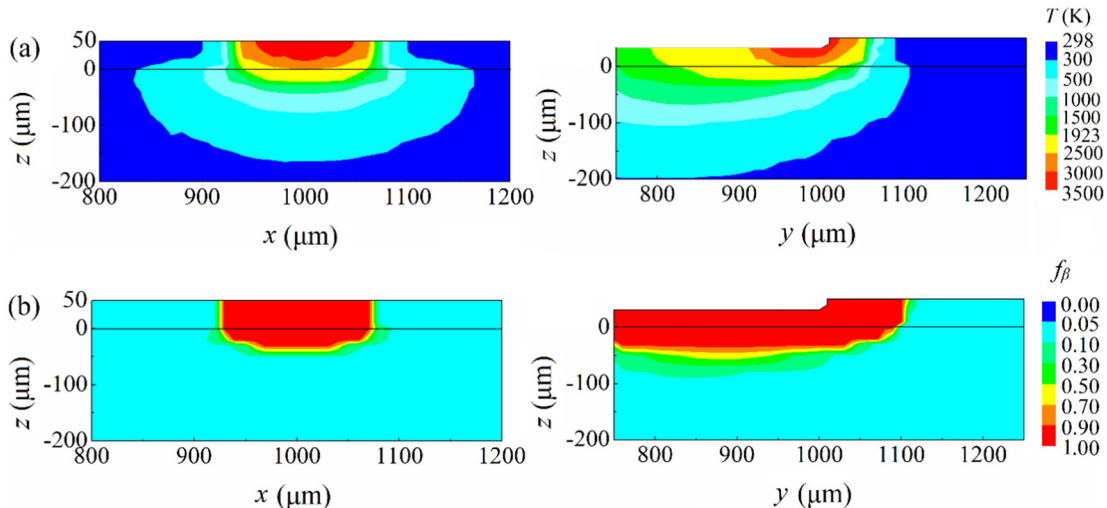


**Fig. 12.** (a) Temperature and (b)  $\beta$  phase fields in the  $x$ - $z$  and  $y$ - $z$  cross sections for a one-track printing process.

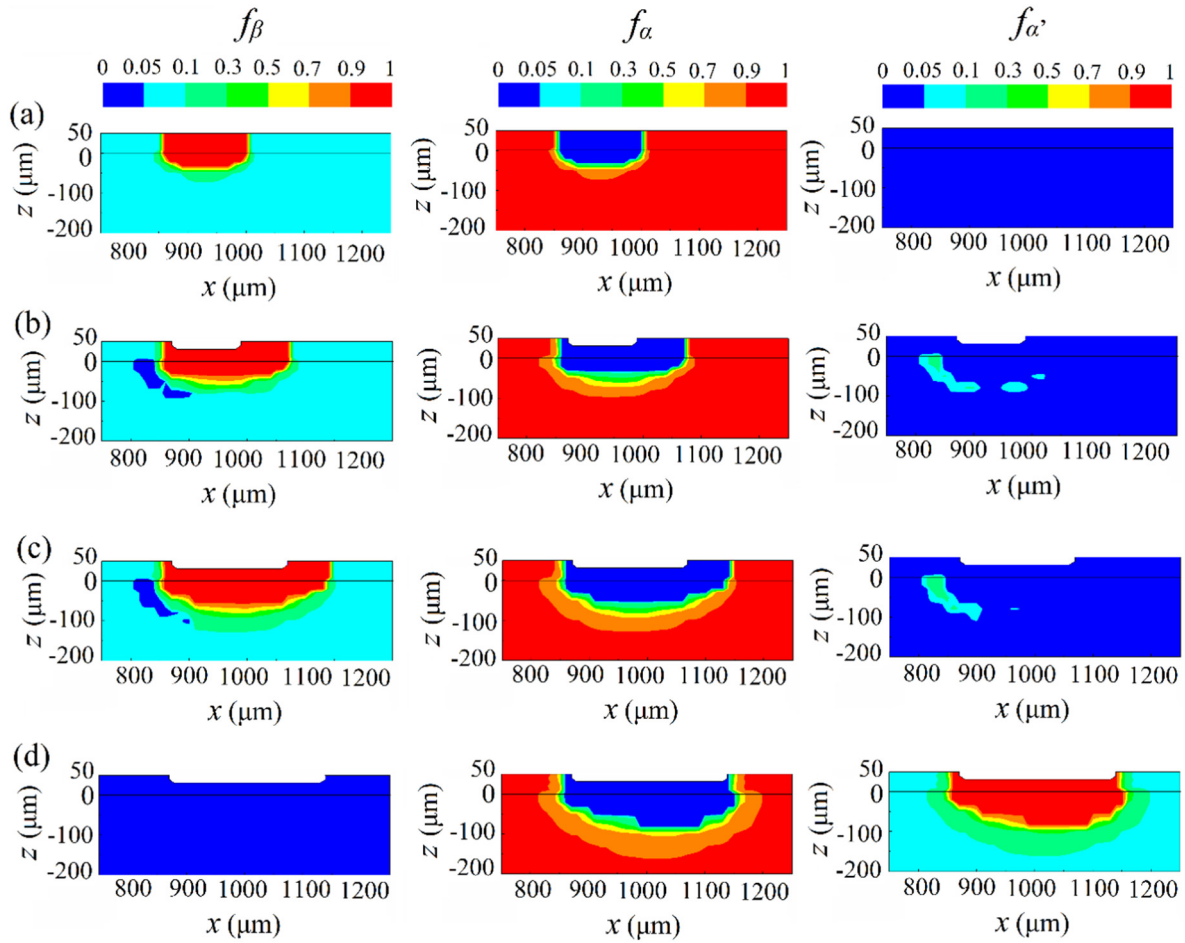


Fig. 13. Solid-state phase fields for a three-track printing process in the  $x$ - $z$  cross section at the different time: (a) first track, (b) second track, (c) third track and (d) after cooling down.

where  $u$ ,  $v$  and  $w$  are the displacements in the  $x$ ,  $y$  and  $z$  directions, respectively;  $W$ ,  $L$  and  $H$  are the length, width and height of the substrate plate, respectively.

Fig. 15 illustrates the comparison of von Mises stress fields without and with the SSPT for the one-layer printing process at different instances of time. The printing time  $t_m$  of the one-layer eight-track printing process is  $6.67 \times 10^{-3}$  s. The printed part approaches the ambient

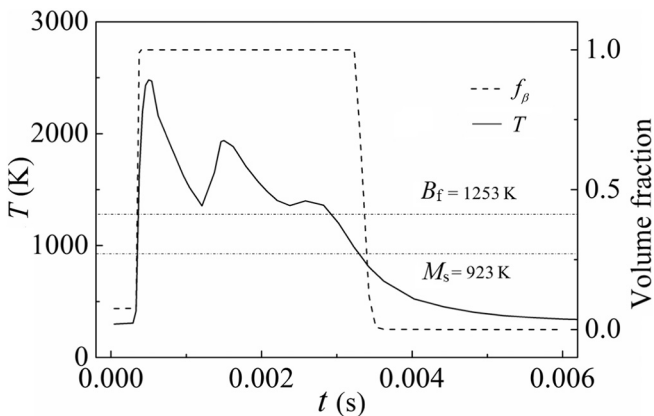


Fig. 14. Evolution of the (a) temperature and (b) phase volume fraction  $f_\beta$  for a three-track printing process.

temperature  $T_\infty = 298$  K after 500 s of cooling. Fig. 15(a) gives the von Mises stress fields when one half of the powder bed is scanned by the laser beam. The grey part represents deactivated fresh powder particles which have no influence on the mechanical analysis of the printed part. The blue region has a low stress level because this region is the melt pool where the Young's modulus and yield stress are assumed to be very small. A large stress occurs at the first-track region at the end of the laser scanning process as shown in Fig. 15(b), which is caused by the formation of tensile residual stresses after the laser beam moves away. The von Mises stress increases as the temperature declines during the cooling process, as given in Fig. 15(c) and (d). The large stress is distributed along the scanning track because these regions suffer from high temperature gradients, which is consistent with the reported results in [10,43].

Fig. 15 also shows that the stress level with the SSPT is smaller than that without the SSPT during laser scanning and cooling processes. This can be explained by the volume change schematic due to the SSPT as shown in Fig. 1. The material volume decreases during the heating process and increases during the cooling process, which is different from the thermal expansion and contraction caused by the temperature change. As a result, the SSPT and thermal gradients have an opposite effect on the evolution of the thermal stress field.

Residual stress components with and without the SSPT for the one-layer printed part are demonstrated in Fig. 16. Compared with the other two stress components  $\sigma_x$  and  $\sigma_z$ , the stress component  $\sigma_y$  has the maximum stress because the scanning

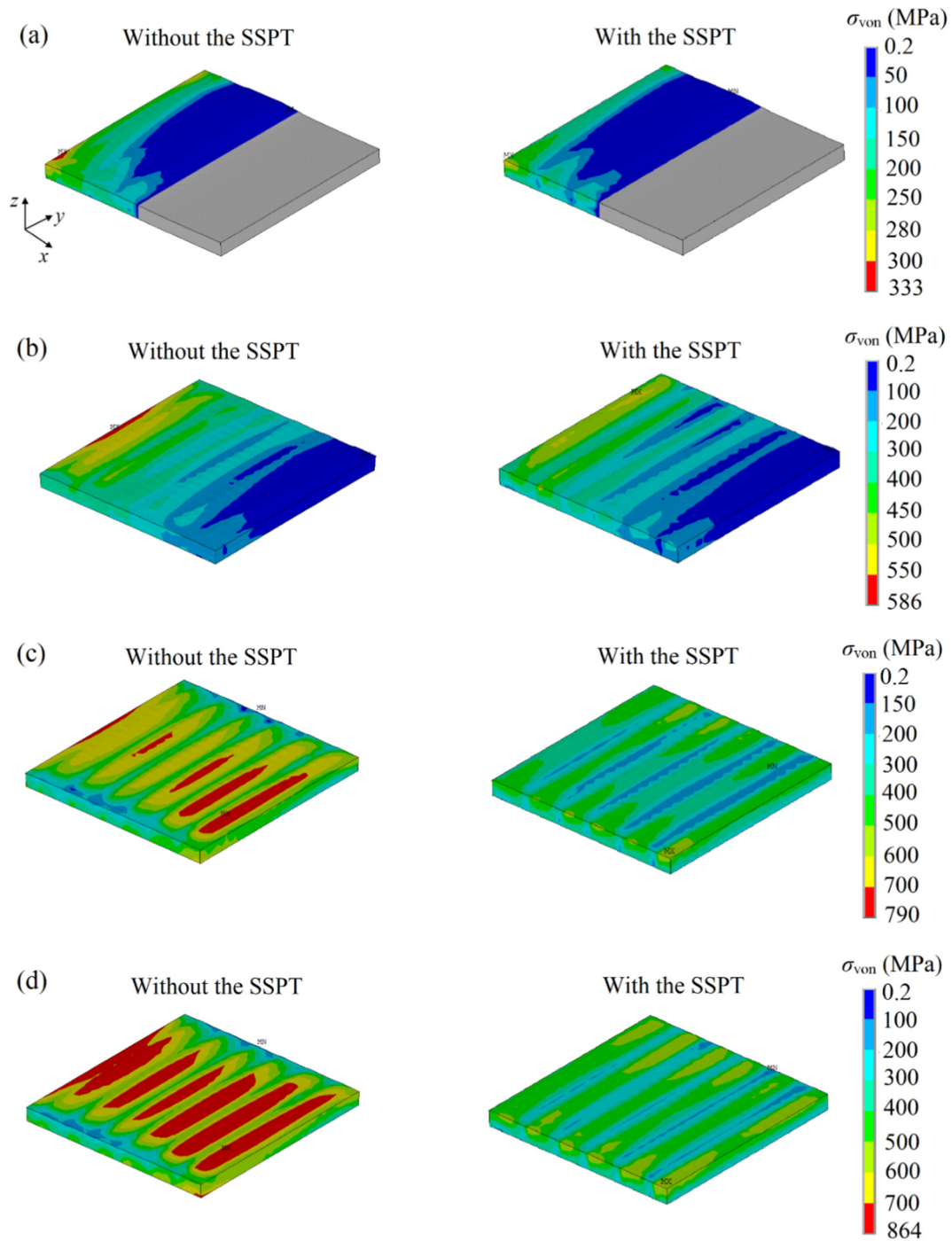


Fig. 15. Evolution of von Mises stress fields with and without the SSPT for the one-layer printing process: (a)  $t_m/2$ , (b)  $t_m$ , (c)  $t_m + 1$  and (d)  $t_m + 500$ .

direction is in the  $y$  direction such that the newly printed part is constrained by previously printed parts. Hence, we can see that a large stress value occurs along the scanning track. Furthermore, the  $z$ -direction stress component is smaller than the other two stress components because of the free constraint on the top surface. For stress components  $\sigma_x$ ,  $\sigma_y$  and  $\sigma_z$ , the tensile stress level with the SSPT is larger than those without the SSPT, which is consistent with the comparison of von Mises stress fields in Fig. 15. In addition, larger compressive stresses are observed when the SSPT is considered.

The significance of the SSPT has been proved from the stress fields in the one-layer printing process. In this case, residual stress fields for a four-layer printed part with consideration of the SSPT are presented. The FEM model and printing process parameters are given in Fig. 10 and Table 1, respectively. The residual stress component  $\sigma_y$  and von Mises stress  $\sigma_{von}$  for a four-layer printed part are shown in Fig. 17. For the stress component  $\sigma_y$ , the maximum tensile and compressive stresses occur at the bottom and top surfaces, respectively. To observe the stress fields in the thickness direction, the residual stress field in the  $x$ - $z$  cross section at the center of the four-layer printed part is given. The stress

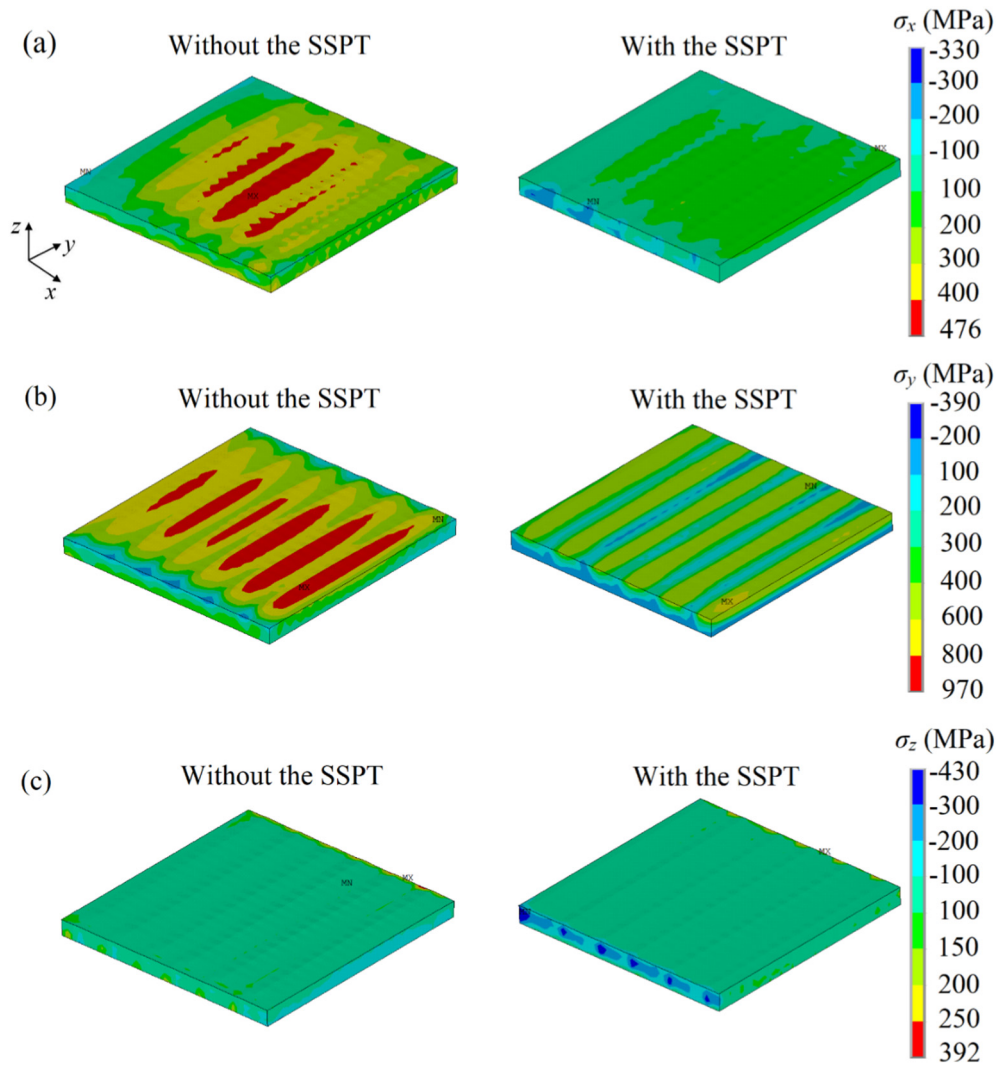


Fig. 16. Residual stress fields with and without the SSPT for the one-layer printed part: (a)  $\sigma_x$ , (b)  $\sigma_y$  and (c)  $\sigma_z$ .

components  $\sigma_y$  has tensile stress in the first three layers and compressive stress at the fourth-layer region. Fig. 17(b) shows that the maximum von Mises stress is at the bottom just like the stress component  $\sigma_y$  and the minimum stress is at the middle region, which is also observed in other reported simulation results [7,8]. In addition, the maximum stress in the four-layer printed part (871 MPa) is larger than the maximum von Mises stress of the one-layer part (606 MPa).

#### 4. Conclusions

Despite great advances in the thermo-mechanical modelling of the SLM process, a comprehensive understanding of thermal and mechanical behaviours with consideration of the phase transformation phenomena is rarely reported. Hence, this work investigates the thermo-metallurgical-mechanical behaviours of the Ti6Al4V product manufactured by SLM technique. The sequentially coupling model which consists of thermal, metallurgical and mechanical analyses aims at predicting the temperature, solid-phase and stress fields during the SLM process. The effects of the repeated SSPT on residual stress fields in the multi-track multi-layer process has been studied based on the developed model. The modelling results show that consideration of the SSPT gives rise to the decrease of tensile residual stresses and the increase of compressive residual stresses. For a one-layer printed part,

the stress component in the scanning direction is larger than the other two stress components. In a four-layer printed part, the maximum von Mises stress is located at the bottom region.

The thermo-metallurgical-mechanical coupling model is a useful tool in process parameter optimization for improving dimensional accuracy and mechanical performance of SLM-printed products. Besides, the multi-track multi-layer model can also be extended to predict residual stresses of complex practical components fabricated by the laser additive manufacturing process.

#### Author contributions

P. Tan developed the model, conducted simulation and analysis, and wrote the manuscript. K. Zhou initiated the idea, analyzed the results and worked on the manuscript. F. Shen analyzed the results and worked on the manuscript. B. Li analyzed the results and worked on the manuscript.

#### Acknowledgements

The authors would like to acknowledge the financial support from the National Research Foundation Medium Sized Center, Singapore through the Marine and Offshore Program.

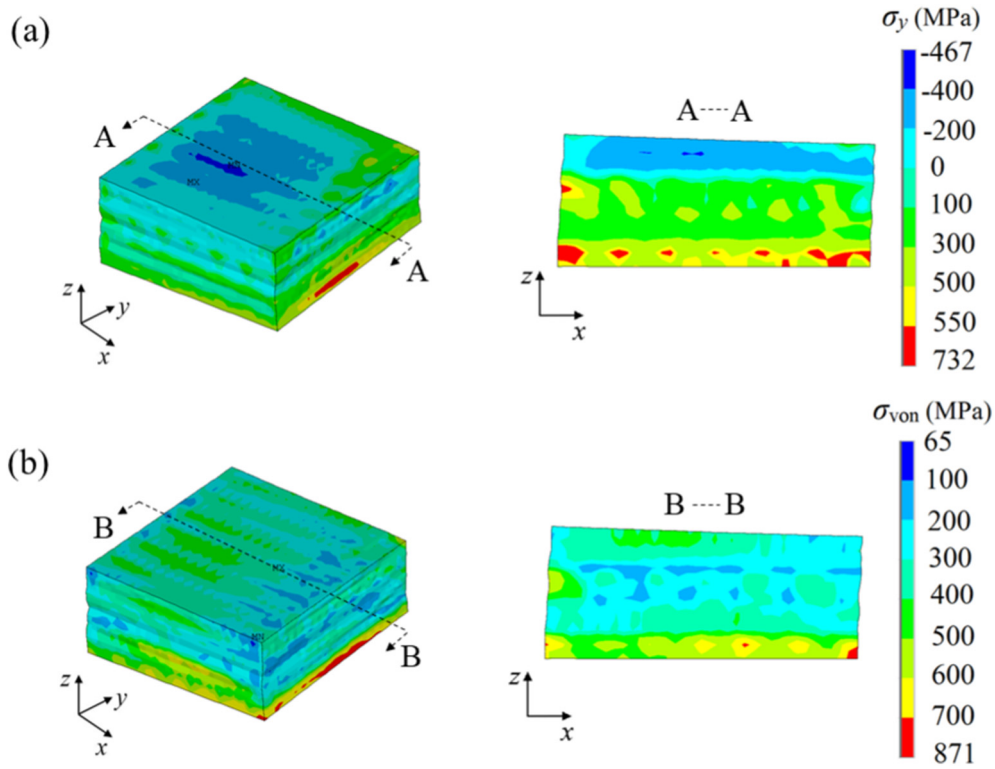


Fig. 17. Residual stress fields for a four-layer printed part with the SSPT: (a)  $\sigma_y$  and (b)  $\sigma_{von}$ .

**Appendix A. Flowchart for a thermo-metallurgical-mechanical coupling model for the SLM process**

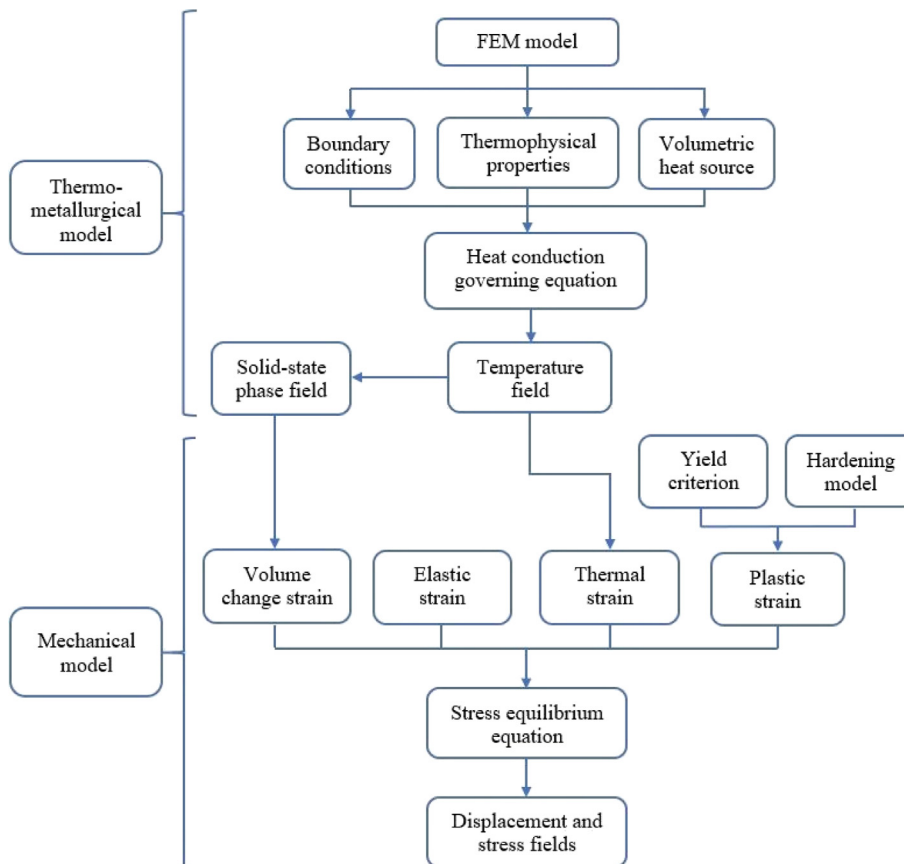


Fig. A1. Flowchart of a thermo-metallurgical-mechanical coupling model for the SLM process.

A flowchart to describe the coupling model for analyzing residual stresses in the SLM process is illustrated in Fig. A1. The heat absorbed from the laser beam diffuses through heat conduction in the powder bed and substrate, heat convection in the melt pool, and air convection and radiation with the ambient environment. The thermal model is based on the heat conduction governing equation because heat conduction occupies a main role in the instantaneous diffusion of heat. The air convection and radiation are considered as boundary conditions. A volumetric heat source is used to represent the interaction between the laser beam and powder particles due to the porosity of the powder bed. The volume fractions of solid-state phases during the heating and cooling processes are predicted by semi-empirical formulas which are a function of the temperature. The temperature and solid-state phase fields are imported into the mechanical analysis model to obtain the thermal strain and volumetric change strain, respectively. Finally, an elasto-plastic constitutive relationship considering the thermal strain and volumetric change strain is proposed to evaluate stress fields.

## Appendix B. Normalized laser irradiance $q$ for the volumetric heat source

By solving the radiation transfer equation in the thickness direction of the powder bed, the normalized laser irradiance  $q$  is given as [31]:

$$q(\xi) = \frac{\eta a}{(4\eta - 3)D} (1 - \eta^2) e^{-\lambda} \left[ (1 - a) e^{-2a\xi} + (1 + a) e^{2a\xi} \right] - (3 + \eta e^{-2\lambda}) \times [1 + a - \eta(1 - a)] e^{2a(\lambda - \xi)} + [1 - a - \eta(1 + a)] e^{2a(\lambda - \xi)} - \frac{3(1 - \eta)(e^{-\xi} - \eta e^{\xi - 2\lambda})}{4\eta - 3} \quad (B1)$$

$$D = (1 - a)[1 - a - \eta(1 + a)] e^{-2a\lambda} - (1 + a)[1 + a - \eta(1 - a)] e^{2a\lambda}, \quad (B2)$$

where  $\eta$  is the hemispherical reflectivity of powder particles,  $a = \sqrt{1 - \eta}$ , and the optical thickness  $\lambda = \gamma L$  with  $L$  being the thickness of the powder layer.

## References

- [1] T. DebRoy, H.L. Wei, J.S. Zuback, T. Mukherjee, J.W. Elmer, J.O. Milewski, A.M. Beese, A. Wilson-Heid, A. De, W. Zhang, Additive manufacturing of metallic components – process, structure and properties, *Prog. Mater. Sci.* 92 (2018) 112–224.
- [2] P. Mercelis, J.P. Kruth, Residual stresses in selective laser sintering and selective laser melting, *Rapid Prototyp. J.* 12 (5) (2006) 254–265.
- [3] N.E. Hodge, R.M. Ferencz, J.M. Solberg, Implementation of a thermomechanical model for the simulation of selective laser melting, *Comput. Mech.* 54 (1) (2014) 33–51.
- [4] I. Yadroitsev, I. Yadroitsava, Evaluation of residual stress in stainless steel 316L and Ti6Al4V samples produced by selective laser melting, *Virtual Phys. Prototyp.* 10 (2) (2015) 67–76.
- [5] Y. Li, K. Zhou, P. Tan, S.B. Tor, C.K. Chua, K.F. Leong, Modeling temperature and residual stress fields in selective laser melting, *Int. J. Mech. Sci.* 136 (2018) 24–35.
- [6] H. Shipley, D. McDonnell, M. Culleton, R. Coull, R. Lupoi, G. O'Donnell, D. Trimble, Optimisation of process parameters to address fundamental challenges during selective laser melting of Ti-6Al-4V: a review, *Int. J. Mach. Tools Manuf.* 128 (2018) 1–20.
- [7] X. Lu, X. Lin, M. Chiumenti, M. Cervera, J. Li, L. Ma, L. Wei, Y. Hu, W. Huang, Finite element analysis and experimental validation of the thermomechanical behavior in laser solid forming of Ti-6Al-4V, *Addit. Manuf.* 21 (2018) 30–40.
- [8] J. Cao, M.A. Gharghoury, P. Nash, Finite-element analysis and experimental validation of thermal residual stress and distortion in electron beam additive manufactured Ti-6Al-4V build plates, *J. Mater. Process. Technol.* 237 (2016) 409–419.
- [9] T. Furumoto, T. Ueda, A. Aziz, M. Sanusi, A. Hosokawa, R. Tanaka, Study on reduction of residual stress induced during rapid tooling process: influence of heating conditions on residual stress, *Key Eng. Mater.* (2010) 785–789.
- [10] L. Parry, I. Ashcroft, R.D. Wildman, Understanding the effect of laser scan strategy on residual stress in selective laser melting through thermo-mechanical simulation, *Addit. Manuf.* 12 (2016) 1–15.
- [11] M.F. Zaeh, G. Branner, Investigations on residual stresses and deformations in selective laser melting, *Prod. Eng.* 4 (1) (2009) 35–45.
- [12] H. Ali, H. Ghadbeigi, K. Mumtaz, Effect of scanning strategies on residual stress and mechanical properties of selective laser melted Ti6Al4V, *Mater. Sci. Eng. A* 712 (2018) 175–187.
- [13] C. Li, C.H. Fu, Y.B. Guo, F.Z. Fang, A multiscale modeling approach for fast prediction of part distortion in selective laser melting, *J. Mater. Process. Technol.* 229 (2016) 703–712.
- [14] T. Mukherjee, W. Zhang, T. DebRoy, An improved prediction of residual stresses and distortion in additive manufacturing, *Comput. Mater. Sci.* 126 (2017) 360–372.
- [15] L. Costa, R. Vilar, T. Reti, A.M. Deus, Rapid tooling by laser powder deposition: process simulation using finite element analysis, *Acta Mater.* 53 (14) (2005) 3987–3999.
- [16] J.W. Elmer, T.A. Palmer, S.S. Babu, W. Zhang, T. DebRoy, Phase transformation dynamics during welding of Ti-6Al-4V, *J. Appl. Phys.* 95 (12) (2004) 8327–8339.
- [17] Y. Fan, P. Cheng, Y.L. Yao, Z. Yang, K. Eglund, Effect of phase transformations on laser forming of Ti-6Al-4V alloy, *J. Appl. Phys.* 98 (1) (2005), 013518.
- [18] C.-H. Lee, K.-H. Chang, Finite element simulation of the residual stresses in high strength carbon steel butt weld incorporating solid-state phase transformation, *Comput. Mater. Sci.* 46 (4) (2009) 1014–1022.
- [19] M. Zain-ul-abdein, D. Nélias, J.-F. Jullien, F. Boitout, L. Dischert, X. Noe, Finite element analysis of metallurgical phase transformations in AA 6056-T4 and their effects upon the residual stress and distortion states of a laser welded T-joint, *Int. J. Press. Vessel. Pip.* 88 (1) (2011) 45–56.
- [20] M.R. Allazadeh, C.I. Garcia, FEM technique to study residual stresses developed in continuously cast steel during solid–solid phase transformation, *Ironmak. Steelmak.* 38 (8) (2013) 566–576.
- [21] D. Deng, FEM prediction of welding residual stress and distortion in carbon steel considering phase transformation effects, *Mater. Des.* 30 (2) (2009) 359–366.
- [22] A. Suárez, M.J. Tobar, A. Yáñez, I. Pérez, J. Sampedro, V. Amigó, J.J. Candel, Modeling of phase transformations of Ti6Al4V during laser metal deposition, *Phys. Procedia* 12 (2011) 666–673.
- [23] J. Yang, H. Yu, J. Yin, M. Gao, Z. Wang, X. Zeng, Formation and control of martensite in Ti-6Al-4V alloy produced by selective laser melting, *Mater. Des.* 108 (2016) 308–318.
- [24] H. Ali, H. Ghadbeigi, K. Mumtaz, Residual stress development in selective laser-melted Ti6Al4V: a parametric thermal modelling approach, *Int. J. Adv. Manuf. Technol.* 97 (5–8) (2018) 2621–2633.
- [25] R. Filip, K. Kubiak, W. Ziąja, J. Sieniawski, The effect of microstructure on the mechanical properties of two-phase titanium alloys, *J. Mater. Process. Technol.* 133 (1–2) (2003) 84–89.
- [26] J. Ahn, E. He, L. Chen, R.C. Wimpory, J.P. Dear, C.M. Davies, Prediction and measurement of residual stresses and distortions in fibre laser welded Ti-6Al-4V considering phase transformation, *Mater. Des.* 115 (2017) 441–457.
- [27] T. Ahmed, H. Rack, Phase transformations during cooling in  $\alpha + \beta$  titanium alloys, *Mater. Sci. Eng. A* 243 (1–2) (1998) 206–211.
- [28] W. Xu, M. Brandt, S. Sun, J. Elambasseril, Q. Liu, K. Latham, K. Xia, M. Qian, Additive manufacturing of strong and ductile Ti-6Al-4V by selective laser melting via in situ martensite decomposition, *Acta Mater.* 85 (2015) 74–84.
- [29] S. Lu, M. Qian, H. Tang, M. Yan, J. Wang, D. StJohn, Massive transformation in Ti-6Al-4V additively manufactured by selective electron beam melting, *Acta Mater.* 104 (2016) 303–311.
- [30] H. Carslaw, J. Jaeger, *Conduction of Heat in Solids*, Oxford Science Publications, Oxford, England, 1959.
- [31] A.V. Gusarov, I. Yadroitsev, P. Bertrand, I. Smurov, Model of radiation and heat transfer in laser-powder interaction zone at selective laser melting, *J. Heat Transf.* 131 (7) (2009), 072101.
- [32] M. Avrami, Kinetics of phase change. II transformation-time relations for random distribution of nuclei, *J. Chem. Phys.* 8 (2) (1940) 212–224.
- [33] G. Krauss, Deformation and fracture in martensitic carbon steels tempered at low temperatures, *Metall. Mater. Trans. A* 32 (4) (2001) 861–877.
- [34] D. Koistinen, R. Marbürger, A general equation prescribing extent of austenite-martensite transformation in pure Fe-C alloy and plain carbon steels, *Acta Metall.* 7 (1) (1959) 59–60.
- [35] S.H. Cho, J.W. Kim, Analysis of residual stress in carbon steel weldment incorporating phase transformations, *Sci. Technol. Weld. Join.* 7 (4) (2013) 212–216.
- [36] J.W. Elmer, T.A. Palmer, S.S. Babu, E.D. Specht, In situ observations of lattice expansion and transformation rates of  $\alpha$  and  $\beta$  phases in Ti-6Al-4V, *Mater. Sci. Eng. A* 391 (1–2) (2005) 104–113.
- [37] A. Hussein, L. Hao, C. Yan, R. Everson, Finite element simulation of the temperature and stress fields in single layers built without-support in selective laser melting, *Mater. Des.* 52 (2013) 638–647.
- [38] K. Dai, L. Shaw, Thermal and mechanical finite element modeling of laser forming from metal and ceramic powders, *Acta Mater.* 52 (1) (2004) 69–80.
- [39] R. Rai, J.W. Elmer, T.A. Palmer, T. DebRoy, Heat transfer and fluid flow during key-hole mode laser welding of tantalum, Ti-6Al-4V, 304L stainless steel and vanadium, *J. Phys. D: Appl. Phys.* 40 (18) (2007) 5753–5766.
- [40] K.C. Mills, Recommended Values of Thermophysical Properties for Selected Commercial Alloys, Woodhead Publishing Ltd, 2002.
- [41] V. Bobkov, L. Fokin, E. Petrov, V. Popov, V. Rumiantsev, A. Savvatimsky, Thermophysical Properties of Materials for Nuclear Engineering: A Tutorial and Collection of Data, IAEA, Vienna, 2008.
- [42] F. Verhaeghe, T. Craeghs, J. Heulens, L. Pandraers, A pragmatic model for selective laser melting with evaporation, *Acta Mater.* 57 (20) (2009) 6006–6012.
- [43] S. Tadano, T. Hino, Y. Nakatani, A modeling study of stress and strain formation induced during melting process in powder-bed electron beam melting for Ni superalloy, *J. Mater. Process. Technol.* 257 (2018) 163–169.